

Contents lists available at [ScienceDirect](https://www.sciencedirect.com)

Journal of Sound and Vibration

journal homepage: www.elsevier.com/locate/jsv

Numerical and experimental study of impact dynamics of bistable buckled beams

Michael Rouleau, James Keller, Jason Lee, Steven Craig, Chengzhi Shi, Julien Meaud*

George W. Woodruff School of Mechanical Engineering, Georgia Institute of Technology, United States of America

ARTICLE INFO

Keywords:

Bistability
Impact excitation
Buckled beam
Contact

ABSTRACT

Bistable systems have been of great research interest due to their rich dynamics arising from a variety of excitations. This study presents an investigation into the nonlinear dynamics of a continuous bistable beam subjected to a form of vibro-impact forcing. A fixed-fixed Euler-Bernoulli beam, precompressed to achieve bistability, is considered, while a shaker with sinusoidally-prescribed velocity applies transverse impact forcing. By varying excitation parameters such as frequency and amplitude, the system response can be tuned. The study begins by employing a Galerkin expansion to the continuous equation of motion, using the buckling modes to remove buckling level dependence and ensure equilibrium symmetry. A Hertzian contact law is chosen to model the collision between the shaker and the buckled beam. The rich dynamics of this system are then explored through numerical and experimental analyses. The focus lies on investigating the emergence of intrawell and interwell dynamics that arise with varying excitation frequency, amplitude, and location. Moreover, we evaluate the significance of including higher-order modes in the modeling of bistable beam dynamics, particularly near snapthrough. This research provides valuable insights into the behavior of continuous bistable structures under vibro-impact forcing, contributing to the understanding and control of such systems in engineering applications.

1. Introduction

Bistable systems, which have two stable equilibria, allow for the design of unique control and memory processes [1,2]. These systems can be found in electrical, mechanical, optical, and even biochemical domains [3–6]. Their multi-stable nature allows for the design of flip-flop circuits, relaxation oscillators [7], Schmitt triggers [8], energy harvesters with increased bandwidth [9,10], and even controllable hysteresis [8,11]. Mechanical bistabilities in particular have garnered interest recently in soft robotics, where they are used for energy absorption, sensing, logical computation, and building metamaterials [12].

Mechanical systems can be discrete, and even single degree of freedom devices can be bistable [13–15]. However, more general continuous systems allow more complex realistic mechanisms to be analyzed. This is particularly useful when dealing with complex geometries and some types of excitation, such as impact, which require the consideration of higher order modes [16]. Complex bistable mechanisms under external excitation often occur within the energy harvesting literature [17–19]. However, these structures are often simplified to few degrees of freedom for convenience [20]. In addition, base excitation is typical for these applications. In the sensing literature, more complex excitation may be present, including contact, but the analyses are often limited to quasi-static time scales [21].

* Corresponding author.

E-mail address: julien.meaud@me.gatech.edu (J. Meaud).

<https://doi.org/10.1016/j.jsv.2024.118291>

Received 27 June 2023; Received in revised form 8 December 2023; Accepted 18 January 2024

Available online 19 January 2024

0022-460X/© 2024 Elsevier Ltd. All rights reserved.

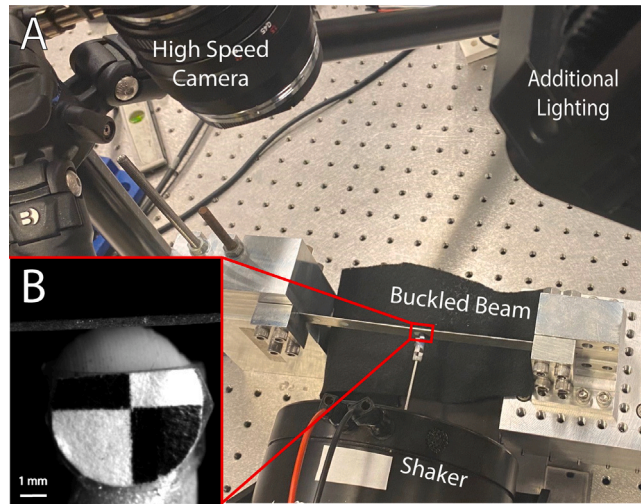


Fig. 1. A: Experimental Setup with high speed camera and clamped–clamped buckled beam. A shaker with a rounded tip provides excitation. A laser doppler vibrometer (not pictured) records shaker velocity. B: An example frame from the high speed camera. Shaker and beam displacement are extracted from these frames. The sticker near the tip of the shaker aids this computational object tracking.

Another common form of excitation for mechanical systems is impact. Impact dynamics is a vast area of research spanning hundreds of years and numerous applications across physics and engineering such as the modeling of ideal gases and robotics. From the discrete discontinuities proposed by Newton [22] to the contact-impact law proposed by Hertz [23], a number of models have been proposed to describe collisions between bodies as a function of velocity [24], geometry, and other parameters. These impacts create discontinuities in the response of the bodies, which arise in the field of nonsmooth mechanics [25,26]. Especially for continuous systems, discontinuities may create rich dynamics [27] as grazing bifurcations emerge. Further, since each set of impact conditions may not be known *a priori*, limited analysis tools are available. However, some systems may benefit from piecewise linear analysis [28] and collocation methods [29], which can significantly ease the computational burden. Even when contact is not intermittent, nonlinear contact laws give rise to distortion of the response waveform [30,31].

The rich impact dynamics may also be applied to fundamentally nonlinear (e.g. bistable) systems, where the limitations in analytical techniques becomes even more pronounced. Nevertheless, impact in bistable systems has received increasing attention for applications in energy harvesting [32,33], load protection [34], and metamaterials [35]. The snapthrough event itself has also been shown to generate an impulse-like excitation, exciting higher-order modes [36].

Lacking from literature, however, are fundamental investigations into a single continuous bistable system excited solely via impact. These investigations would facilitate intimate understanding of the underlying dynamics of a nonlinear system excited via contact, which can be generalized to many other systems.

While our previous work [13], has focused on the rich dynamics arising in a SDOF bistable system excited via impact, we now extend this investigation by considering a continuous bistable structure under vibro-impact forcing. We present numerical and experimental representations of a fixed–fixed Euler–Bernoulli beam which is precompressed to achieve bistability and provide a shaker with sinusoidally-prescribed velocity for transverse impact forcing. The nonlinear nature of the system allows for tuning of the rich system responses by varying excitation parameters. In this case, by changing the excitation frequency, amplitude, and location, different responses are possible, including intrawell and interwell responses. Comparison to a SDOF system highlights unique characteristics of these tunable responses in a 32 mode approximation of a continuous buckled beam.

2. Experimental methods

Experimentally, the buckled beam is represented as a slender beam constructed of mild steel and fixed in a custom compression fixture seen in Fig. 1A. First, the beam is fixed at each end by the even clamping of 4 bolts torqued to 15 N-m each. This fixed–fixed beam is then precompressed and buckled via a leadscrew, creating a bistable energy profile with equi-level energy minima. This symmetry was validated by testing the natural frequency of the first dynamic mode about both equilibria; natural frequencies of 81.3 Hz and 80.5 Hz indicate good symmetry. A B&K Type 4809 shaker with a custom aluminum and polylactic acid stinger rod placed near the center of the span provides transverse impact excitation at frequencies between 20 Hz and 300 Hz for 200 cycles. A Polytec PDV-100 laser doppler records shaker velocity within $1.7 \mu\text{m/s}$. A signal to noise ratio of $>15 \text{ dB}$ for all experiments indicate near-sinusoidal motion. Simultaneously, a 10,000 fps Photron camera records position of the shaker and beam around the point of excitation with the help of an external LED light. The camera records the image with a pixel size of $12 \mu\text{m}$. Each frame (e.g. Fig. 1B) is processed using a custom binarization and object tracking code written in Python using OpenCV [37,38] to extract the location of the shaker and beam simultaneously. After each experiment, the beam and shaker are reset to their initial static configuration before the next experiment.

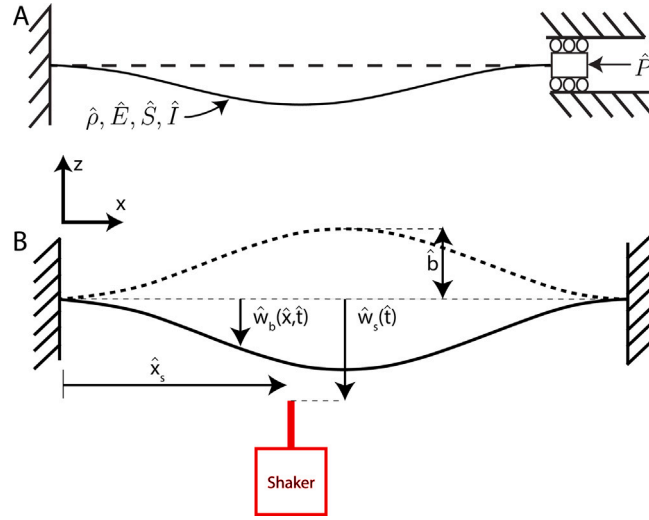


Fig. 2. A schematic of the bistable beam system showing the buckled beam (black) and shaker (red). During interwell motion, the beam moves from the first stable equilibrium (solid) to the second stable equilibrium (dashed). (For interpretation of the references to color in this figure legend, the reader is referred to the web version of this article.)

By varying shaker amplitude and frequency, a variety of responses are observed including intrawell, transient intrawell, and continuous interwell as described in Section 4. These dynamics have the potential to vary across large ranges of excitation parameters, which can be experimentally difficult to achieve. Further, key information about modal amplitudes and contact forces can be challenging to measure experimentally while simultaneously capturing the displacement and contact of two bodies. These constraints motivate us to develop a computational model of the system.

3. Model description

3.1. Beam model

The model begins with the forced equation of motion [39,40] for the transverse displacement \hat{w} of an undamped beam of length \hat{L} that undergoes compression under an axial load \hat{P} (Fig. 2), which is given by:

$$\hat{\rho}\hat{S}\frac{\partial^2\hat{w}_b}{\partial\hat{t}^2} + \hat{E}\hat{I}\frac{\partial^4\hat{w}_b}{\partial\hat{x}^4} + \left[\hat{P} - \frac{\hat{E}\hat{S}}{2\hat{L}}\int_0^{\hat{L}}\left(\frac{\partial\hat{w}_b}{\partial\hat{x}}\right)^2d\hat{x}\right]\frac{\partial^2\hat{w}_b}{\partial\hat{x}^2} = \hat{f}(\hat{t})\delta(\hat{x}_s). \quad (1)$$

Important system parameters include the beam density $\hat{\rho}$, Young's modulus \hat{E} , moment of inertia \hat{I} , and cross-sectional area \hat{S} where the $\hat{\cdot}$ indicates dimensional quantities. $\hat{f}(\hat{t})$ is a transverse point force located at \hat{x}_s , which represents the system excitation. Note that the time-dependence of $\hat{f}(\hat{t})$ is implicit; it arises from the time-dependence of the shaker displacement, and will be further discussed in Section 3.2.

Nayfeh et al. [39] have shown that \hat{P} significantly affects the natural frequencies of the system. \hat{P} can be directly calculated by measuring the buckling level \hat{b} , which is defined in Fig. 2. This buckling level, *i.e.* the apex height of the buckled beam, is given by:

$$\hat{b} = \sqrt{\frac{4\hat{L}^2}{\pi^2\hat{E}\hat{S}}(\hat{P} - \hat{P}_{cr})}, \quad (2)$$

where the first critical buckling load is

$$\hat{P}_{cr} = \frac{4\pi^2\hat{E}\hat{I}}{\hat{L}^2}. \quad (3)$$

The dynamic modes can be used as a basis to project the displacement of the beam from its initial symmetric buckled state as done by Emam et al. [41]. However, the projection based on dynamic modes results in a bistable system with stable equilibria at different energy levels. This is because the initial shape of a buckled beam cannot be exactly represented by a truncated sum of dynamic modes. To avoid this, we use the buckling modes $\hat{\phi}_i(\hat{x})$ given by Timoshenko and Gere [42] as an orthogonal basis for our Galerkin expansion. These modes are given by:

$$\hat{\phi}_i(\hat{x}) = \hat{A}_i \sin(\hat{k}_i\hat{x}) + \hat{B}_i \cos(\hat{k}_i\hat{x}) + \hat{C}_i\hat{x} + \hat{D}_i, \quad (4)$$

where application of the idealized fixed–fixed boundary conditions

$$\hat{\phi}(\hat{x}) = \frac{\partial \hat{\phi}(\hat{x})}{\partial \hat{x}} = 0 \text{ at } \hat{x} = 0 \text{ and } \hat{x} = \hat{L} \tag{5}$$

leads to solutions for \hat{A}_i , \hat{B}_i , \hat{C}_i , and \hat{D}_i by solving the system of equations

$$\begin{Bmatrix} 0 \\ 0 \\ 0 \\ 0 \end{Bmatrix} = \begin{bmatrix} 0 & 1 & 0 & 1 \\ \hat{k} & 0 & 1 & 0 \\ \sin(\hat{k}\hat{L}) & \cos(\hat{k}\hat{L}) & \hat{L} & 1 \\ \hat{k} \cos(\hat{k}\hat{L}) & -\hat{k} \sin(\hat{k}\hat{L}) & 1 & 0 \end{bmatrix} \begin{Bmatrix} \hat{A} \\ \hat{B} \\ \hat{C} \\ \hat{D} \end{Bmatrix}. \tag{6}$$

We find that \hat{k}_i satisfies

$$\hat{k}_{2i-1} = \frac{2i\pi}{\hat{L}}, \text{ or } \tan\left(\frac{\hat{k}_{2i}\hat{L}}{2}\right) = \frac{\hat{k}_{2i}\hat{L}}{2}, \text{ where } i = 1, 2, 3, \dots, \tag{7}$$

for the symmetric (odd) and antisymmetric (even) buckling modes, respectively. For example, the first buckling mode is given by:

$$\hat{\phi}_1(\hat{x}) = \hat{B}_1 \left[1 - \cos\left(\frac{2\pi\hat{x}}{\hat{L}}\right) \right]. \tag{8}$$

The modes were normalized using the equation

$$\int_{\hat{x}=0}^{\hat{L}} \hat{\phi}'_i(\hat{x})\hat{\phi}'_j(\hat{x})d\hat{x} = \hat{\delta}_{ij}, \tag{9}$$

where ' refers to the derivative with respect to \hat{x} and $\hat{\delta}_{ij}$ the Kronecker delta. This normalization was chosen rather the more conventional normalization with respect to the mass terms as it allows us to greatly simplify the expression for the nonlinear term in the system of ODEs.

The solution is projected onto the buckling modes,

$$\hat{w}_b(\hat{x}, \hat{t}) = \sum_{j=1}^N \alpha_j(\hat{t})\hat{\phi}_j(\hat{x}), \tag{10}$$

which allows the equation of motion to be reduced to the following system of nonlinear ODEs:

$$\sum_{j=1}^N \hat{m}_{ij}\ddot{\alpha}_j + \hat{K}_i^0\alpha_i(\hat{t}) + \left[\sum_{k=1}^N \alpha_k(\hat{t})^2 \right] \hat{\gamma}\alpha_i(\hat{t}) = \hat{f}_i(\hat{t}) \text{ for } i=1,2,\dots, N \tag{11}$$

where the modal force $\hat{f}_i(\hat{t})$ for a point force at \hat{x}_s is given by:

$$\hat{f}_i(\hat{t}) = \hat{\phi}_i(\hat{x}_s)\hat{f}(\hat{t}). \tag{12}$$

The modal mass matrix is given as

$$\hat{m}_{ij} = \hat{\rho}\hat{S} \int_0^{\hat{L}} \hat{\phi}_i(\hat{x})\hat{\phi}_j(\hat{x})d\hat{x} \tag{13}$$

and the linear stiffness is

$$\hat{K}_i^0 = \hat{E}\hat{I} \int_0^{\hat{L}} \hat{\phi}_i''^2(\hat{x})d\hat{x} - \hat{P}. \tag{14}$$

Nonlinear coupling stiffness takes the form

$$\hat{\gamma} = \frac{\hat{E}\hat{S}}{2\hat{L}}. \tag{15}$$

Note that due to the selection of buckling modes, the mass matrix \hat{m}_{ij} is a symmetric checkerboard-patterned matrix. This indicates that this formulation contains linear mass coupling between symmetric modes and between antisymmetric modes, but not between symmetric and antisymmetric modes. However, there is nonlinear elastic coupling between symmetric and antisymmetric modes due to the nonzero $\hat{\gamma}$ term.

3.2. Excitation model

The shaker is modeled as an intermittently contacting discrete point with the velocity

$$\hat{w}_s(\hat{t}) = V\hat{b}\hat{\omega}_1 \cos(\hat{\omega}\hat{t}) \text{ for } \hat{t} \geq 0, \tag{16}$$

where V is the non-dimensional velocity amplitude. The shaker is initially in contact with the beam *i.e.* $\hat{w}_s(0) = \hat{w}_b(\hat{x}_s, 0)$.

A common contact model which has been successfully used in related work [13] is the Newtonian coefficient of restitution (COR) model, which relates the relative velocity of the shaker and beam before and after impact. For SDOF approximations, this relation

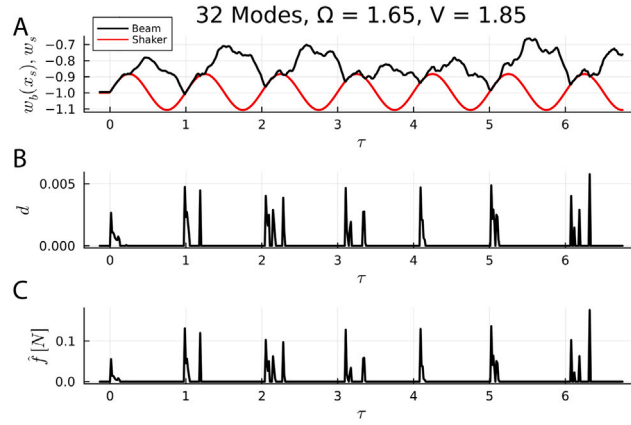


Fig. 3. A: An example simulated waveform of the beam (black) and shaker (red). B: Shallow penetration where a Hertzian contact law is applied. C: The resulting contact force. (For interpretation of the references to color in this figure legend, the reader is referred to the web version of this article.)

is sufficient to model a wide range of collisions. However, for a multi-DOF system, the instantaneous nature of the COR model combined with point excitation does not allow for convergence. Further, the instantaneous nature of the impact does not allow time for waves to propagate in the beam. Thus, a contact model which takes into account the finite duration of contact is required for proper representation of the continuous beam.

Assuming no plastic deformation and small deformation during contact, the model chosen is a Hertzian contact law. While originally developed for a sphere impacting an infinite half-space, Hertz-based contact has been successfully applied to approximate impact in beams for decades (e.g. [43], but also [44–49]). While other contact models may represent the contact mechanics in greater fidelity (e.g. [50,51]), the impulse-like nature of the Hertzian contact law phenomenologically captures the dynamics of the system while limiting free parameters. The contact force is then given as:

$$\hat{f}(\hat{t}) = \hat{f}(\hat{d}(\hat{t})) = \begin{cases} \hat{k}_c [\hat{d}(\hat{t})]^{3/2}, & \text{if } \hat{d}(\hat{t}) \geq 0 \\ 0, & \text{otherwise} \end{cases} \quad (17)$$

where $\hat{d}(\hat{t})$ is the penetration depth given by

$$\hat{d}(\hat{t}) = \hat{w}_s(\hat{t}) - \hat{w}_b(\hat{x}_s, \hat{t}), \quad (18)$$

which can be seen in Fig. 3A when the shaker and beam waveforms cross. The penetration depth in panel B then informs the contact force in panel C. Varying the contact stiffness \hat{k}_c term allows for fine tuning of the collision model for a wide variety of systems.

An immediate consequence of this contact model is that the force applied to the beam is dependent on the displacement of the beam at the location of excitation. This creates an additional form of nonlinear modal coupling that occurs only during contact via the \hat{d} term in Eq. (17).

In both simulation and experiment, the beam initially starts at rest snapped downwards around the stable equilibrium and in contact with the shaker (i.e. $\hat{w}_s(0) = \hat{w}_b(\hat{x}_s, 0) = \alpha_1(0)\hat{\phi}_1(\hat{x})$ where $\alpha_1(0) = -\frac{\hat{b}}{\hat{\phi}_1(\hat{L}/2)}$).

For generalization of model results, normalization is conducted such that $w = \frac{\hat{w}}{\hat{b}}$, $d = \frac{\hat{d}}{\hat{b}}$, $x_s = \frac{\hat{x}_s}{\hat{L}}$, and τ refers to the number of cycles of excitation ($\tau = \frac{t\hat{\omega}}{2\pi}$). The normalized excitation frequency is $\Omega = \frac{\hat{\omega}}{\hat{\omega}_1}$, where $\hat{\omega}_1$ is the first natural frequency of the beam around a stable equilibrium. For the selected buckling level, $\hat{\omega}_1$ also corresponds to the first symmetric dynamic mode. However, for higher buckling levels, the first symmetric dynamic mode may be the second mode of the system [39] and this normalization may no longer be appropriate. For this investigation, simulations with the 32 mode model show $\frac{\hat{\omega}_1}{2\pi} \approx 81.8$ Hz, $\frac{\hat{\omega}_2}{2\pi} \approx 159$ Hz, and $\frac{\hat{\omega}_3}{2\pi} \approx 380$ Hz; the maximum excitation frequency used in the simulations is $\frac{\hat{\omega}_{max}}{2\pi} \approx 325$ Hz.

3.3. Parameter selection

The numerical system parameters were selected to represent the slender steel beam used in experiment. A density of 7800 kg/m³ and a Young's modulus of 200 GPa were used. The beam has a length of 16.1 cm and a rectangular cross-section of thickness \hat{h} and depth 15 mm. \hat{h} was adjusted in the model to match the natural frequencies of the experimental beam prior to compression. While the physical beam thickness measured 0.44 mm, a thickness of 0.4 mm was used *in silico* to exactly match the first two natural frequencies of the experimental straight beam (80 Hz and 221 Hz). The buckling level, \hat{b} , which was measured to be 0.5 mm, was adjusted to 0.335 mm in the simulations in order to obtain near perfect agreement between model and experiments for the 1st

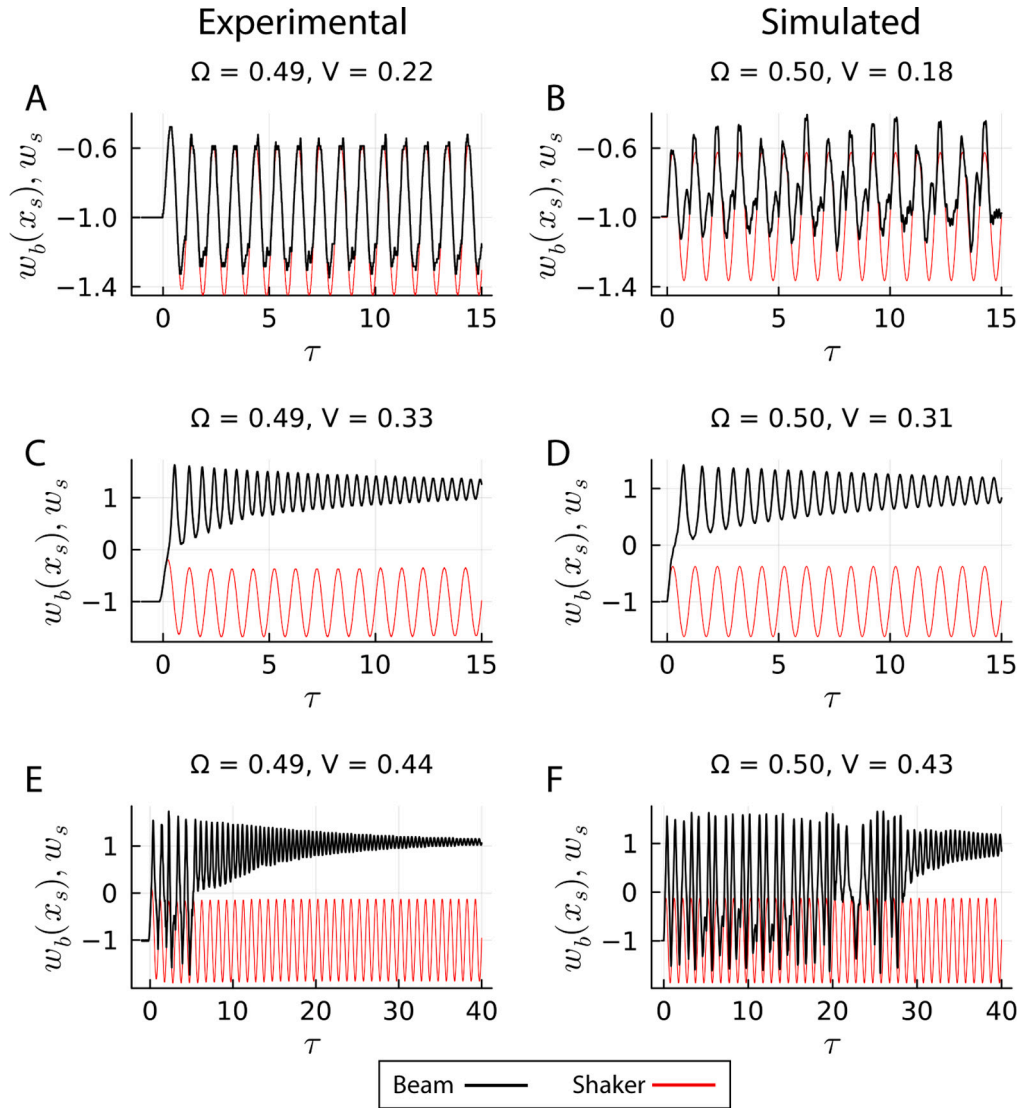


Fig. 4. Beam (black) and shaker (red) displacement waveforms. A, C, E: Experimental, B, D, F: Simulated at similar parameters. A–B: non-periodic intrawell, C–D: transient interwell with multiple snapthroughs. Animations of the simulations are found in Supplemental Information. (For interpretation of the references to color in this figure legend, the reader is referred to the web version of this article.)

natural frequency of the buckled beam (81.8 Hz in both equilibria of the model vs 81.3 Hz and 80.5 Hz in the two equilibria in the experiments).

Unless otherwise noted, excitation is exerted at the point $\hat{x}_s = \hat{L}/2.1$, which is consistent with the experimental location. Finally, light modal damping is introduced to the model; a damping ratio of 0.005 was chosen to match the decay observed in experimental free vibration waveforms. This ratio is used for all modes for simplicity.

The contact stiffness parameter $\hat{k}_c = 4e8 \text{ N/m}^{3/2}$ is calculated using the material properties of the beam and by approximating the collision as a 5 mm diameter polylactic acid sphere on a semi-infinite steel domain to utilize the classical relation described by Hertz [52].

The discretized model was implemented using a Tsitouras 5/4 Runge–Kutta method with automatic stiffness-based switching to an Order 2/3 L-Stable Rosenbrock–W method from the DifferentialEquations.jl [53] package in the Julia programming language [54].

The number of modes used in this analysis ($N = 32$) was determined by a qualitative convergence study over the wide range of excitation frequencies and amplitudes described in the results. For $N = 32$, the natural frequencies of the first 10 dynamic modes were found to be accurate to within 0.07% of the exact analytical values described by Nayfeh et al. [39] (see Appendix A). A single mode model is used as comparison to the converged 32 DOF model.

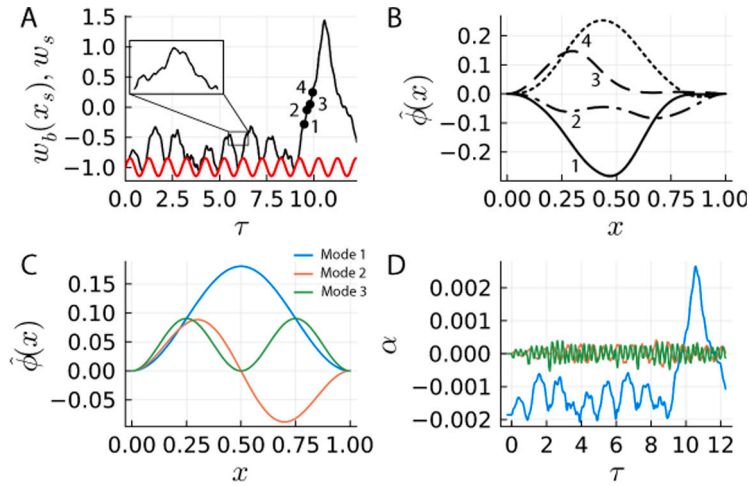


Fig. 5. A: A waveform with snapthrough at $\Omega = 1.21$, $V = 0.18$. B: Snapshots the beam snapping through at the times indicated in panel A. C: First 3 buckling modes. D: Modal amplitudes. During snapthrough (e.g. at points 2 and 3), the response is dominated by higher order modes (i.e. mode 2, 3, 4...).

4. Results

4.1. Comparison of model and experimental waveforms

Over a wide range of excitation frequencies and amplitudes, we observe qualitative agreement between experimental and simulated results, as shown by the representative waveforms in Fig. 4 for both experiment (left column) and simulation (right column). The first row of the figure is a case of a low shaker velocity input, where the beam remains in the neighborhood of the initial equilibrium, i.e., $w_b(x_s, t) \approx -1$ (intrawell response). In panels A & B, the response appears non-periodic and is of similar but not identical amplitude. For the second row, the peak shaker velocity is increased, but the excitation frequency is kept constant. Here, both panel C & D exhibit a transient interwell response, where the beam snaps between equilibria a finite number of times. In these examples, only one snapthrough occurs. Often, these responses are characterized by decaying oscillations around the second equilibrium, which we term transient interwell 2. However, it is also possible for a transient interwell response to return to an orbit around the first equilibrium in a transient interwell 1 response. The third row (panels E & F) exhibits another example of transient interwell responses, where multiple snapthroughs occur before the beam finds stability around an equilibrium. Again, this stability is often characterized by convergence to the second equilibrium. While the experimental shaker's motion exhibits minimal distortion, a short transient response is present before steady state, which has the potential to significantly alter the observed response. For example, the first cycle of the excitation waveform in panel C is larger than the steady state amplitude. This transient response, combined with imperfections in the impact model, boundary conditions, etc., largely limit our agreement to a qualitative comparison. Additionally, slight differences in the initial conditions and successive impacts have the potential to significantly influence the beam response, particularly in regions of non-periodicity or near transitions between response types.

In experiment, the excitation amplitude and frequency range is limited. However, the system can be explored more thoroughly using the computational model. In addition, we can more easily explore a critical defining feature of this continuous system: the influence of higher order modes.

4.2. Effects of higher-order modes

Compared to a SDOF approximation, a continuous system exhibits several unique response characteristics. For example, there often exists an anti-symmetric contribution that is prominent during snapthrough during both quasistatic [55] and dynamic responses. In Fig. 5, a relatively large asymmetric component emerges during snapthrough when the first modal amplitude is near 0 (e.g. see points 2 and 3 in Fig. 5). This means that for any bistable beam that may snap through, inclusion of these higher-order modes is crucial for the modeling of accurate system dynamics. Away from the unstable equilibrium, the first mode grows, quickly dominating over the antisymmetric contributions.

In the special case where excitation is provided at the center of the beam, there is no direct excitation of the antisymmetric modes. However, for off-center excitation, all modes are excited, either directly or via modal coupling. These modes then remain critical for modeling accurate system dynamics for the next impact, as they directly influence contact force and timing and therefore energy transfer.

Another effect of higher order modes is the emergence of high-frequency oscillations in the free-vibration portion of the response. For displacement at the center of the beam, this effect is attributed to the odd modes, which are all dynamically coupled. For example,

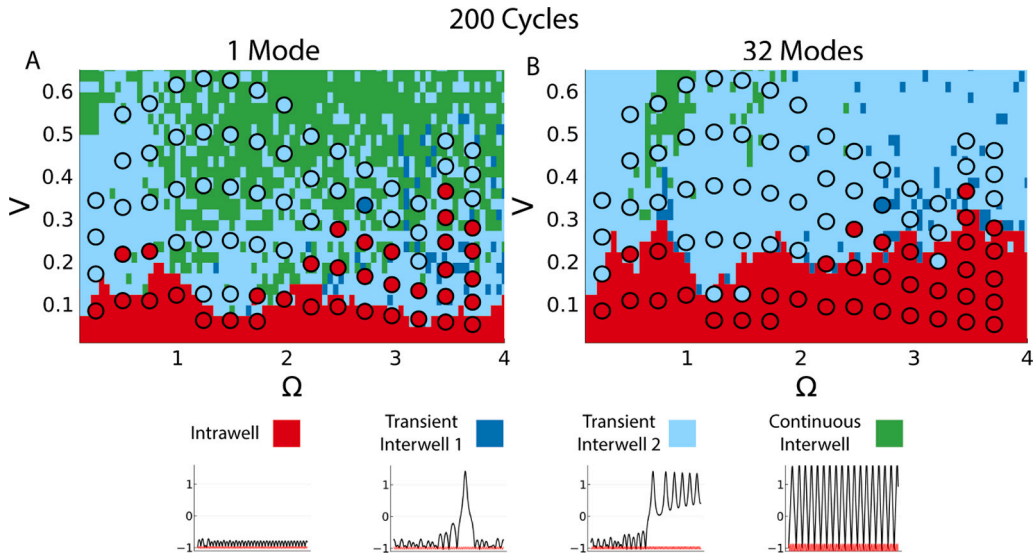


Fig. 6. Simulated and experimental responses across a wide range of excitation parameters. Response types determined following 200 cycles of excitation. Dot overlay indicates experimental measurements. A: 1 mode model. B: 32 mode model response.

the inset of Fig. 5A displays high frequency oscillations during every cycle. This response is also apparent in the modal amplitudes in Fig. 5D; the magnified response in panel A corresponds to contributions primarily from the first few modes in panel D.

One benefit of computational exploration is the ability to efficiently model and analyze large ranges of system parameters. For this investigation, we increase the simulated parameter range beyond the experimental range, up to $\Omega = 4$ and $V = 0.65$ as in Figs. 6 and 7. The resulting responses are categorized into interwell (blue and green) and intrawell (red) responses based on whether the displacement at the center of the beam passes the unstable equilibrium (i.e. contains a zero crossing). To determine the difference between continuous (green) and transient (blue) interwell responses, we look at the last quarter of the simulated duration ($n = 50$ cycles in Fig. 6, $n = 250$ cycles in Fig. 7). If the number of zero crossings is greater than $n/5$, the response is determined to be continuous interwell. For Fig. 6, this translates to 10 zero crossings over the last 50 cycles of excitation; Fig. 7 requires 50 zero crossings over the last 250 cycles of excitation. Two types of transient interwell responses were identified depending of the type of response at the end of the simulation: transient interwell 1 (dark blue) and transient interwell 2 (light blue).

On this more global scale, as excitation frequency and amplitude are varied in Fig. 6, the differences in response type between SDOF and 32 DOF become apparent. While both models are strikingly similar to the response of another impact-forced bistable system [13], in Fig. 6, the 32 mode fine structure in panel B is more sharply tuned than the single mode model in panel A. The notch near $\Omega = 1.4$, which has been linked to system resonance [13] in an SDOF model, shifts lower in the 32 DOF model to $\Omega \approx 1.2$. However, experiment shows a notch closer to $\Omega = 1.4$. This resonance effect can also be observed as frequency is swept for low amplitude excitation in Appendix B. At high frequency, the velocity amplitude required to achieve snapthrough in a single mode model remains relatively low while the 32 mode model threshold continues to rise gradually. Additionally, this threshold amplitude is universally higher in the 32 mode model and is more consistent with experiment. Overall, the SDOF model predicts the frequencies of experimental threshold minima, but the 32 mode model represents a much better estimation of the threshold amplitude across all frequencies to within 1 experimental data point. As noted previously, approximations in the model (particularly the contact model), inconsistent initial conditions, and a transient response in the experimental excitation likely contribute to these differences in experimental responses.

Comparing Figs. 6 and 7, the system's transient response exceeds 200 excitation cycles (and thus the experimental limits) for many parameter combinations. In particular, the 32 mode system converges to entirely transient interwell 2 responses for high V/Ω combinations, while transient interwell 1 responses all but disappear for the SDOF model. This extended transient response may also extend beyond 1000 cycles, particularly for non-periodic simulations near the snapthrough threshold amplitude and nonperiodic transient interwell 1 responses.

At very low frequency, the SDOF model of the beam is expected to snap through when the maximum shaker displacement goes past the unstable equilibrium of the beam, i.e.,

$$w_{s,max} > 0, \quad (19)$$

which can be written as

$$V > -\Omega w_b(x_s, 0). \quad (20)$$

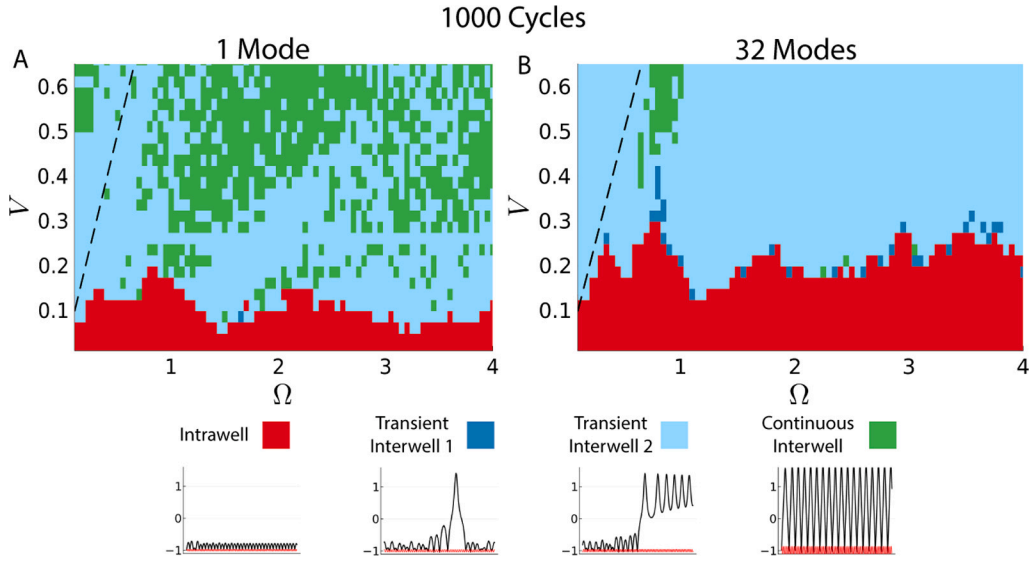


Fig. 7. Simulated and experimental responses after 1000 cycles of excitation. Dashed black lines indicate the SDOF threshold given by Eq. (21). A: 1 mode model. B: 32 mode model. While most snapthrough events in the 32 mode model result in a transient interwell response, many continuous interwell responses may be stable in the 1 mode model.

This inequality is used to define the SDOF quasi-static velocity threshold:

$$V_{QS1}(x_s, \Omega) = -\Omega w_b(x_s, 0) = \frac{\Omega \hat{\phi}_1(x_s)}{\hat{\phi}_1(0.5)} \quad (21)$$

At low frequencies, the boundary between intrawell and interwell responses in SDOF and 32 mode models seems to converge to this threshold, which corresponds to the black dashed line in Fig. 7; however, at higher frequencies, interwell responses are observed at velocity V significantly lower than $V_{QS1}(x_s, \Omega)$, which means that the shaker does not need to move past the unstable equilibrium of the beam to cause snap-through.

4.3. Changing shaker location

Another distinctive difference between SDOF and 32 DOF approximations emerges when the excitation location is varied as illustrated in Fig. 8A. Note that the shaker begins in contact with the beam, regardless of shaker position.

In the SDOF model, Eq. (21) predicts that the velocity threshold between intrawell and interwell response is proportional to $\hat{\phi}_1(x_s)$, which is observed not only at low frequency in Fig. 8B, but also at higher frequencies in panels D and F. At low frequency, the threshold between intrawell and interwell responses closely follows the $V = 1 \times V_{QS1}(x_s, \Omega)$ line, which is the expected quasistatic response for the SDOF system. At higher frequencies, the velocity amplitude threshold required to achieve snapthrough is also nearly proportional to the $V = V_{QS1}(x_s, \Omega)$ line, albeit at a much lower amplitude ($V = 0.2 \times V_{QS1}(x_s, \Omega)$ in panel D and $V = 0.05 \times V_{QS1}(x_s, \Omega)$ in panel F).

The threshold of the 32 mode model also follows the equation the $V = 1 \times V_{QS1}(x_s, \Omega)$ line trend in the case of the very low frequency excitation ($\Omega = 0.05$ in Fig. 8C). However, the 32 mode model significantly deviates from the trend expected for the SDOF model at $\Omega = 0.625$ in panel E. The model exhibits a broad peak in the threshold for $x_s \approx 0.4$. Excitation of higher order modes significantly increase the snap-through threshold for all shaker locations, with a more pronounced effect for $x_s \approx 0.4$ than for shaker locations either the boundary or center of the beam. This effect is even more apparent at excitation frequencies above $\Omega = 1$, as in panel G, where the 32 mode model threshold increases for a large range of shaker locations around $x_s \approx 0.3$. Experimental results collected for $\Omega = 1.625$ demonstrate a similar increase in the threshold for $x_s \approx 0.3$ in manner roughly consistent with the 32 mode model.

The number of modes N used in our reduced order model was systematically varied from 1 to 32 to study the influence of N on the map of Fig. 8 at $\Omega = 1.625$. The results of this study, which are shown in Supplemental Video SI5, show a significant increase in the threshold around $x_s \approx 0.25$ as soon as $N = 2$ modes are considered. This location corresponds roughly to the location of the antinode of the 2nd mode, $x \approx 0.3$. The rise in the threshold at this location arises because the shaker provides energy not only to the first mode, which can directly leads to snap-through of the beam, but also to the 2nd mode, which is not associated with snap-through. Introducing higher order progressively cause small changes in the map. However, the map obtained with $N = 16$ modes is nearly identical to the map with $N = 32$ modes, demonstrating near convergence of the results.

Further analysis of Fig. 8 provides a set of trade-offs that are present in selecting an excitation location for efficient snapthrough. In a SDOF approximation, the threshold velocity amplitude required to achieve snapthrough is proportional to the $V = V_{QS1}(x_s, \Omega)$

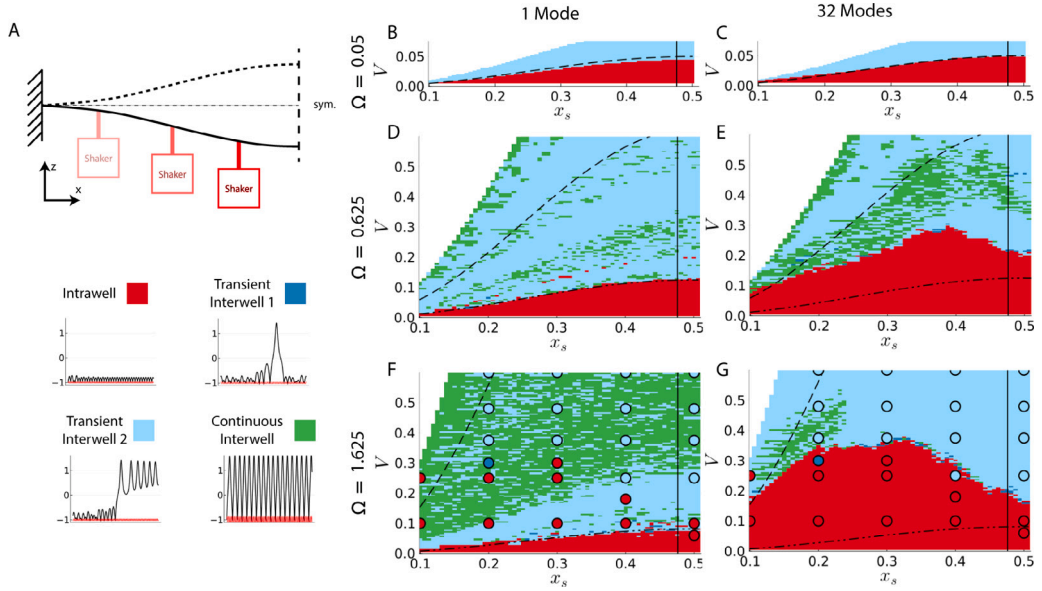


Fig. 8. Major response types as shaker location is varied. A: Schematic showing possible initial configurations. The shaker starts in contact with the buckled beam, regardless of x_s . B, D, & F: 1 mode. C, E, & G: 32 modes. For all panels, results are limited to $V < 2 \times V_{QS1}(x_s, \Omega)$; the curve $V = 1 \times V_{QS1}(x_s, \Omega)$ is plotted in black dashes; vertical line at $x_s = 1/2.1$ indicates shaker location in prior figures. Panels B & C ($\Omega = 0.05$) thresholds closely follow the $V = 1 \times V_{QS1}(x_s, \Omega)$ line. The boundary between intrawell and interwell responses in panels D & E ($\Omega = 0.625$) are significantly below the $1 \times V_{QS1}$ line. The threshold between intrawell and interwell responses predicted by the 1 mode model is much lower than the 32 modes; furthermore, the 32 mode model threshold displays a broad notch when x_s is near the center of the beam. The 1 mode model follows the curve $V = 0.2 \times V_{QS1}(x_s, \Omega)$, which is plotted in black dash-dot in D & E. Panels F & G ($\Omega = 1.625$) further highlight the model differences as the 1 mode model threshold lowers and follows the curve $V = 0.05 \times V_{QS1}(x_s, \Omega)$, plotted in black dash-dot, while the 32 mode model threshold increases for much of the beam and the notch near the center deepens. Dot overlay in panels F&G indicates experimental measurements.

line in panels B, D, & F, regardless of excitation frequency. In the 32 mode model which is a better approximation of the continuous system, the threshold curve follows a more complicated pattern. The threshold velocity reaches a broad maximum around $x_s = 0.3$ to 0.4 depending on the excitation frequencies as shown in panels E, & G. This means that for velocity-constrained excitation, such as those that occur within metamaterials [56] and sensors [1], excitation near either a boundary ($x_s \approx 0$) or the center ($x_s \approx 0.5$) is most efficient, particularly at high frequency. Aside from snapthrough thresholds, there also exists a shift in response type as a function of shaker location. For example, if a transient interwell response is desired, a shaker near the center of the beam has a wide amplitude window available to achieve that response. Near a beam boundary, a shaker requires much finer amplitude control to reliably achieve a transient interwell response.

5. Conclusions

In this work, the fundamental problem of a continuous bistable beam excited by impacts with a sinusoidally vibrating shaker has been explored. Experimental and computational results at a low buckling level support the emergence of rich dynamics that are highly dependent on excitation parameters. Additionally, we show that the inclusion of higher-order modes is critical for modeling bistable beam dynamics near the unstable equilibrium.

We utilize a derivation of a dynamical model based on buckling modes to ensure symmetry of the bistable system. This model is coupled with a Hertzian contact model to simulate a continuous bistable beam under a special form of transverse vibro-impact excitation. Using this model, we uncover rich tunable dynamics with the potential for intrawell, transient interwell, and continuous interwell responses dependent on excitation frequency, amplitude, and position. Additionally, experiments across a range of amplitudes and frequencies qualitatively validate the model, particularly for estimation of the snapthrough threshold.

While a single mode model is adequate for approximating the frequencies of low-amplitude resonances, inclusion of higher-order modes is crucial for estimating the exact threshold amplitude, and for high-frequency excitation.

Additionally, multiple modes are required to accurately model phenomena such as high frequency oscillations and the effects of changing excitation location (the 2nd mode, which is antisymmetric, is especially critical). These effects can be used to tune the system for efficient snapthrough by considering both displacement and force constraints of the excitation.

When excitation location is varied, the effect of multiple modes is further exemplified as changes in the excitation threshold. For low excitation frequencies, threshold curves for the SDOF approximations at a fixed frequency resemble the first buckling mode shape (albeit at different amplitudes). Near the center of the beam, a substantially different threshold shape emerges in the 32 mode approximation and in the experiments.

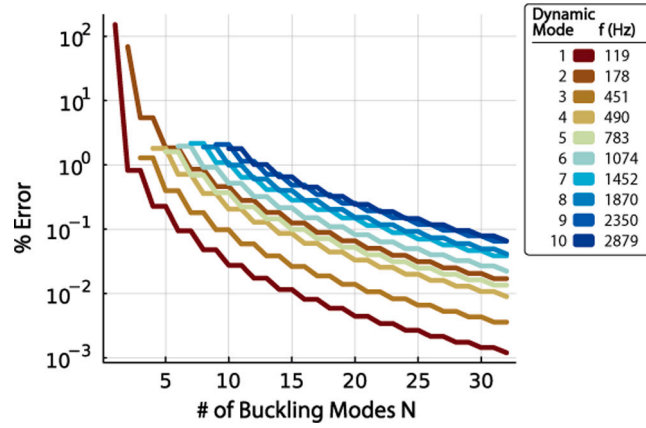


Fig. A.9. Convergence of the natural frequencies of all modes <3 kHz. Dynamic modes are ordered by natural frequency.

CRediT authorship contribution statement

Michael Rouleau: Investigation, Software, Writing – original draft. **James Keller:** Software. **Jason Lee:** Investigation. **Steven Craig:** Investigation. **Chengzhi Shi:** Conceptualization, Funding acquisition, Writing – review & editing. **Julien Meaud:** Conceptualization, Funding acquisition, Supervision, Writing – review & editing.

Declaration of competing interest

The authors declare that they have no known competing financial interests or personal relationships that could have appeared to influence the work reported in this paper.

Data availability

Data will be made available on request.

Acknowledgments

This project was funded by the National Science Foundation, United States of America [grant number CMMI 2037565]. The authors would like to thank Prof. Claudio V. Di Leo for sharing the high speed camera and Prof. Michael Leamy for sharing laboratory equipment.

Appendix A. Eigenfrequency convergence

Since the analytical dynamic modes were not chosen as a basis, an additional investigation was used to confirm convergence to the exact natural frequencies of the system. To find the natural frequencies around the equilibrium of the buckled beam, a solution of the following form is assumed for the unforced version of Eq. (11):

$$\vec{a}(t) = \vec{a}(0) + \delta\vec{a}e^{i\omega t} \quad (\text{A.1})$$

where $\delta\vec{a}$ is a small perturbation from the buckled configuration of the beam; $\vec{a}(0) = [\alpha_1(0), 0, \dots, 0]^T$ where $\alpha_1(0)$ is the modal amplitude of the 1st buckling mode at rest. Keeping only the linear terms in $\delta\vec{a}$ result in the characteristic equation $\det(\hat{K} - \omega_n^2 \hat{m}) = 0$ which is used to find the natural frequencies of the buckled beam. In the characteristic equation, \hat{K} is the diagonal matrix with the following term on the diagonal:

$$\begin{aligned} \hat{K}_{11} &= \hat{K}_1^0 + 3\gamma [\alpha_1(0)]^2 \\ \hat{K}_{ii} &= \hat{K}_i^0 + 2\gamma [\alpha_1(0)]^2 \text{ for } i \neq 1. \end{aligned} \quad (\text{A.2})$$

Limiting our convergence investigation to the first 10 dynamic modes (spanning all natural frequencies below 3 kHz), Fig. A.9 was obtained. Nayfeh et al.'s approach [39] to obtaining the exact analytic buckled beam natural frequencies serves as a theoretical reference for the calculation of relative error.

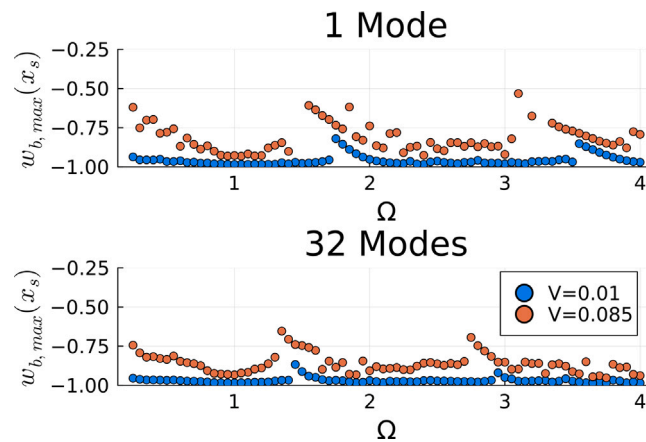


Fig. B.10. Maximum beam displacement over 1000 cycles at the location of excitation as a function of frequency. A: 1 mode approximation. B: 32 mode approximation.

Appendix B. Resonance

As discussed in [13], the presence of notches in the threshold between intrawell and interwell responses (Fig. 6) are linked to resonances of the system. Fig. B.10A illustrates this resonance for a 1 mode approximation at two excitation levels. At low excitation levels, two maximum are observed at $\Omega \approx 1.8$ and $\Omega = 3.6$. At moderate excitation levels, the displacement peak shifts left due to the softening nonlinearity. For a single mode, another local maxima also emerges near $\Omega = 3.5$. In the 32 mode model in Fig. B.10B, these local maxima emerge at lower frequencies.

Appendix C. Supplementary data

Supplementary material related to this article can be found online at <https://doi.org/10.1016/j.jsv.2024.118291>.

References

- [1] K.-W. Wang, R.L. Harne, *Harnessing Bistable Structural Dynamics: For Vibration Control, Energy Harvesting and Sensing*, John Wiley & Sons, 2017.
- [2] R.J. Tseng, J. Ouyang, C.-W. Chu, J. Huang, Y. Yang, Nanoparticle-induced negative differential resistance and memory effect in polymer bistable light-emitting device, *Appl. Phys. Lett.* 88 (12) (2006) 123506.
- [3] P. Pathak, R. Deb, S.R. Mohapatra, Electrical bistability in MoS₂ nano-sheets doped polymeric nanocomposite films, *Mater. Today Proc.* 24 (2020) 2295–2301.
- [4] J.L. Silverberg, J.-H. Na, A.A. Evans, B. Liu, T.C. Hull, C.D. Santangelo, R.J. Lang, R.C. Hayward, I. Cohen, Origami structures with a critical transition to bistability arising from hidden degrees of freedom, *Nat. Mater.* 14 (4) (2015) 389–393.
- [5] L.A. Lugiato, II theory of optical bistability, in: *Progress in Optics*, Vol. 21, Elsevier, 1984, pp. 69–216.
- [6] C. Thron, Bistable biochemical switching and the control of the events of the cell cycle, *Oncogene* 15 (3) (1997) 317–325.
- [7] V. Chickarmane, B.N. Kholodenko, H.M. Sauro, Oscillatory dynamics arising from competitive inhibition and multisite phosphorylation, *J. Theoret. Biol.* 244 (1) (2007) 68–76.
- [8] F. Yuan, Differential CMOS schmitt trigger with tunable hysteresis, *Analog Integr. Circuits Signal Process.* 62 (2010) 245–248.
- [9] R.L. Harne, K. Wang, A review of the recent research on vibration energy harvesting via bistable systems, *Smart Mater. Struct.* 22 (2) (2013) 023001.
- [10] S.P. Pellegrini, N. Tolou, M. Schenk, J.L. Herder, Bistable vibration energy harvesters: a review, *J. Intell. Mater. Syst. Struct.* 24 (11) (2013) 1303–1312.
- [11] H. Chang, H. Wu, C. Xie, H. Wang, Controlled shift of optical bistability hysteresis curve and storage of optical signals in a four-level atomic system, *Phys. Rev. Lett.* 93 (21) (2004) 213901.
- [12] A. Pal, M. Sitti, Programmable mechanical devices through magnetically tunable bistable elements, *Proc. Natl. Acad. Sci.* 120 (15) (2023) e2212489120.
- [13] M. Rouleau, S. Craig, Y. Xia, R. Shieh, M.L. Robinson, C. Shi, J. Meaud, Nonlinear dynamics of a bistable system impacting a sinusoidally vibrating shaker, *Nonlinear Dynam.* (2022) 3015–3030.
- [14] B. Mann, Energy criterion for potential well escapes in a bistable magnetic pendulum, *J. Sound Vib.* 323 (3–5) (2009) 864–876.
- [15] H. Alhoussein, M.F. Daqaq, Potential well escape via vortex-induced vibrations: A single-degree-of-freedom analysis, *Physica D* 426 (2021) 133001.
- [16] R. Szalai, Impact mechanics of elastic structures with point contact, *J. Vib. Acoust.* 136 (4) (2014).
- [17] H. Li, A. Li, X. Kong, Design criteria of bistable nonlinear energy sink in steady-state dynamics of beams and plates, *Nonlinear Dynam.* 103 (2) (2021) 1475–1497.
- [18] A. Amor, A. Fernandes, J. Pouget, Snap-through of elastic bistable beam under contactless magnetic actuation, *Int. J. Non-Linear Mech.* 119 (2020) 103358.
- [19] M.-U. Noll, L. Lentz, U. von Wagner, On the discretization of a bistable cantilever beam with application to energy harvesting, *Facta Univ. Ser. Mech. Eng.* 17 (2) (2019) 125–139.
- [20] S. Shaw, Forced vibrations of a beam with one-sided amplitude constraint: theory and experiment, *J. Sound Vib.* 99 (2) (1985) 199–212.
- [21] B. Camescasse, A. Fernandes, J. Pouget, Bistable buckled beam: Elastica modeling and analysis of static actuation, *Int. J. Solids Struct.* 50 (19) (2013) 2881–2893.
- [22] D. Wagg, A note on coefficient of restitution models including the effects of impact induced vibration, *J. Sound Vib.* 300 (3–5) (2007) 1071–1078.
- [23] K.L. Johnson, One hundred years of hertz contact, *Proc. Inst. Mech. Eng.* 196 (1) (1982) 363–378.

- [24] X. Zhang, L. Vu-Quoc, Modeling the dependence of the coefficient of restitution on the impact velocity in elasto-plastic collisions, *Int. J. Impact Eng.* 27 (3) (2002) 317–341.
- [25] B. Brogliato, B. Brogliato, *Nonsmooth Mechanics*, Vol. 3, Springer, 1999.
- [26] J. Awrejcewicz, C.-H. Lamarque, *Bifurcation and Chaos in Nonsmooth Mechanical Systems*, Vol. 45, World Scientific, 2003.
- [27] E. Van de Vorst, D. Van Campen, A. De Kraker, R. Fey, Periodic solutions of a multi-DOF beam system with impact, *J. Sound Vib.* 192 (5) (1996) 913–925.
- [28] D. Wagg, S. Bishop, Application of non-smooth modelling techniques to the dynamics of a flexible impacting beam, *J. Sound Vib.* 256 (5) (2002) 803–820.
- [29] D. Wagg, A note on using the collocation method for modelling the dynamics of a flexible continuous beam subject to impacts, *J. Sound Vib.* 276 (3–5) (2004) 1128–1134.
- [30] M. Bryant, Non-linear forced oscillation of a beam coupled to an actuator via hertzian contact, *J. Sound Vib.* 99 (3) (1985) 403–414.
- [31] J. Turner, Non-linear vibrations of a beam with cantilever-hertzian contact boundary conditions, *J. Sound Vib.* 275 (1–2) (2004) 177–191.
- [32] Z. Xie, C. Kitio Kwuimy, T. Wang, X. Ding, W. Huang, Theoretical analysis of an impact-bistable piezoelectric energy harvester, *Eur. Phys. J. Plus* 134 (2019) 1–10.
- [33] P. Podder, A. Amann, S. Roy, Combined effect of bistability and mechanical impact on the performance of a nonlinear electromagnetic vibration energy harvester, *IEEE/ASME Trans. Mechatronics* 21 (2) (2015) 727–739.
- [34] Y. Cao, M. Derakhshani, Y. Fang, G. Huang, C. Cao, Bistable structures for advanced functional systems, *Adv. Funct. Mater.* 31 (45) (2021) 2106231.
- [35] R. Fancher, I. Frankel, K. Chin, M.A. Ghanem, B. MacNider, L.S. Shannahan, J.F. Berry, M. Fermin-Coker, A.J. Boydston, N. Boechler, Dependence of the kinetic energy absorption capacity of bistable mechanical metamaterials on impactor mass and velocity, 2023, arXiv preprint arXiv:2301.09149.
- [36] X. Song, H. Liu, Free vibration of bistable clamped-clamped beams: A preliminary study, in: *International Design Engineering Technical Conferences and Computers and Information in Engineering Conference*, Vol. 83969, American Society of Mechanical Engineers, 2020, V007707A036.
- [37] G. Bradski, *The OpenCV Library*, Dr. Dobb's J. Softw. Tools (2000).
- [38] C.R. Harris, K.J. Millman, S.J. van der Walt, R. Gommers, P. Virtanen, D. Cournapeau, E. Wieser, J. Taylor, S. Berg, N.J. Smith, R. Kern, M. Picus, S. Hoyer, M.H. van Kerkwijk, M. Brett, A. Haldane, J.F. del Río, M. Wiebe, P. Peterson, P. Gérard-Marchant, K. Sheppard, T. Reddy, W. Weckesser, H. Abbasi, C. Gohlke, T.E. Oliphant, Array programming with NumPy, *Nature* 585 (7825) (2020) 357–362, <http://dx.doi.org/10.1038/s41586-020-2649-2>.
- [39] A.H. Nayfeh, W. Kreider, T. Anderson, Investigation of natural frequencies and mode shapes of buckled beams, *AIAA J.* 33 (6) (1995) 1121–1126.
- [40] E. Mettler, Dynamic buckling, in: *Handbook of Engineering Mechanics*, McGraw-Hill New York, 1962, pp. 1–62.
- [41] S.A. Emam, A.H. Nayfeh, On the nonlinear dynamics of a buckled beam subjected to a primary-resonance excitation, *Nonlinear Dynam.* 35 (2004) 1–17.
- [42] S.P. Timoshenko, J.M. Gere, *Theory of Elastic Stability*, Courier Corporation, 2009, pp. 54–55.
- [43] H. Wang, X. Yin, Q. Deng, B. Yu, Q. Hao, X. Dong, Experimental and theoretical analyses of elastic-plastic repeated impacts by considering wave effects, *Eur. J. Mech. A Solids* 65 (2017) 212–222.
- [44] E.H. Lee, *The Impact of a Mass Striking a Beam*, American Society of Mechanical Engineers, 1940.
- [45] H. Schwieger, A simple calculation of the transverse impact on beams and its experimental verification: Since central maximum loading on beams by transverse impact is independent of boundary conditions, the integral equation for impact force due to transverse impact can be simplified and thereby facilitate mechanical-loading calculations, *Exp. Mech.* 5 (11) (1965) 378–384.
- [46] A.S. Yigit, A.G. Ulsoy, R. Scott, Spring-dashpot models for the dynamics of a radially rotating beam with impact, *J. Sound Vib.* 142 (3) (1990) 515–525.
- [47] V. Marinca, N. Herisanu, Impact of piecewise energy harvester system of bistable beam with hertzian contact force, in: *Acoustics and Vibration of Mechanical Structures–AVMS-2021: Proceedings of the 16th AVMS, Timișoara, Romania, May 28–29, 2021*, Springer, 2022, pp. 38–47.
- [48] J. Awrejcewicz, O. Saltykova, Y.B. Chebotyrevskiy, V. Krysko, Nonlinear vibrations of the Euler-Bernoulli beam subjected to transversal load and impact actions, *Nonlinear Stud.* 18 (3) (2011).
- [49] A. Bhattacharjee, A. Chatterjee, Transverse impact of a Hertzian body with an infinitely long Euler-Bernoulli beam, *J. Sound Vib.* 429 (2018) 147–161.
- [50] H.M. Lankarani, P. Nikravesh, A contact force model with hysteresis damping for impact analysis of multibody systems, 1990.
- [51] B.-J. Ryu, H.-H. Han, G.-S. Lee, K.-Y. Ahn, C.-R. Lee, Dynamic response analysis of a cantilevered beam due to an elastic impact, *Int. J. Precis. Eng. Manuf.* 11 (2010) 539–547.
- [52] H. Hertz, *Miscellaneous Papers*, Macmillan, 1896.
- [53] C. Rackauckas, Q. Nie, *DifferentialEquations.jl—a performant and feature-rich ecosystem for solving differential equations in Julia*, *J. Open Res. Softw.* 5 (1) (2017).
- [54] J. Bezanson, A. Edelman, S. Karpinski, V.B. Shah, Julia: A fresh approach to numerical computing, *SIAM Rev.* 59 (1) (2017) 65–98.
- [55] P. Cazottes, A. Fernandes, J. Pouget, M. Hafez, Bistable buckled beam: modeling of actuating force and experimental validations, *J. Mech. Des.* 131 (10) (2009).
- [56] N. Saravana Jothi, A. Hunt, Active mechanical metamaterial with embedded piezoelectric actuation, *APL Mater.* 10 (9) (2022) 091117.